Dalton Transactions

PAPER

View Article Online
View Journal | View Issue

Cite this: *Dalton Trans.*, 2025, **54**, 7376

Phase-dependent optical, photocatalytic and capacitive properties of tungsten oxide nanowires

Zeynep Kahraman,[a,b] Ahmet Güngör,[c,d] Merve Buldu-Aktürk,[e] Metin Tan,[b] Emre Alp,*[f] Emre Erdem*[c,d] and Aziz Genç*[g]

Received 26th January 2025,
Accepted 4th April 2025

DOI: 10.1039/d5dt00212e

rsc.li/dalton

Transition metal oxides hold great promise across a wide range of applications due to favorable properties such as high abundance, low toxicity, and excellent stability. Nanoengineering approaches are essential for controlling the structural, optical, and electronic properties of these materials, enabling the achievement of desired characteristics in a cost-effective and environmentally friendly manner. In this study, we synthesize stoichiometric (WO_3) and sub-stoichiometric (WO_{3-x}) tungsten oxide nanowires by controlling their phases and morphologies through the hydrothermal method. This approach allows us to systematically investigate the effects of different phases and oxygen vacancies on the optical properties, as well as on photocatalytic and supercapacitance applications. We use the photodegradation of RhB as a benchmark for photocatalytic activity under various experimental conditions, revealing that oxygen vacancies significantly influence photocatalytic behavior. For example, WO_{3-x} nanowires adsorb/degrade a substantial amount of RhB within short durations under ambient conditions, where WO_3 nanowires are mostly inactive. The addition of H_2O_2 enhances the photocatalytic performance of WO_3 nanowires over 30 minutes, with even better results under low pH conditions with H_2O_2. This study also explores the phase-dependent electrochemical properties of WO_3 and WO_{3-x} nanowires, providing insights into their potential for improved supercapacitor performance by leveraging their complementary properties in symmetric and asymmetric configurations. WO_{3-x}, with a higher density of oxygen vacancies and thinner structure, offers enhanced conductivity and increased active sites for charge storage, resulting in superior specific capacitance and charge retention.

1. Introduction

Interest in technologies such as photocatalysis, supercapacitors, lithium-ion batteries, and solar and fuel cells for clean and renewable energy solutions has been increasing in response to the environmental impacts of rapid industrialization. As pollution accumulates in water sources, the energy required to mitigate this pollution also rises.[1] The efficiency of these technologies depends on the structural, optical, and electronic properties of the materials used. Therefore, nanoengineering approaches are essential for synthesizing materials with well-defined microstructural features that enable desired properties in a cost-effective and environmentally friendly way.

Photocatalysis, which involves using semiconductors to absorb photons and generate excited electrons and holes that can initiate chemical reduction and/or oxidation, is a valuable method for environmental remediation. This approach gained prominence with the pioneering work of Honda and Fujishima on TiO_2, which highlighted the potential of semiconductors in photocatalysis.[2,3] Although TiO_2 remains a benchmark in photocatalytic applications due to its advantageous properties,[4–6] its band gap of 3.0–3.2 eV restricts its activity to the ultraviolet region of the electromagnetic spectrum, which comprises only about 3% of solar light.[7,8] Consequently, there is significant interest in developing highly efficient and stable visible-light-driven semiconductors, which would operate in the visible range that makes up approximately 47% of solar irradiation, for photocatalytic applications.[9,10]

Among various materials used as photocatalysts, tungsten oxide (WO_3) stands out as an ideal candidate for visible-light-driven photocatalysis. This n-type semiconductor has a band gap of 2.5–2.8 eV and is known for its stability at high temperatures, non-toxic nature, ease of synthesis, and remarkable elec-

---

[a] Chemistry Department, Izmir Institute of Technology, 35430 İzmir, Turkey
[b] Photonics Department, Izmir Institute of Technology, 35430 İzmir, Turkey
[c] Faculty of Engineering and Natural Sciences, Sabancı University, Orhanlı, Tuzla, 34956 İstanbul, Turkey. E-mail: emre.erdem@sabanciuniv.edu
[d] Center of Excellence for Functional Surfaces and Interfaces for Nano-Diagnostics (EFSUN), Sabancı University, Orhanlı, Tuzla 34956, Istanbul, Turkey
[e] Helmholtz-Zentrum Berlin für Materialien und Energie GmbH, Berlin, 14109, Germany
[f] Metallurgy and Materials Engineering Department, Bartın University, 74100 Bartın, Turkey. E-mail: emrealp@bartin.edu.tr
[g] Cardiff Catalysis Institute, School of Chemistry, Cardiff University, Cardiff CF10 3AT, UK. E-mail: azizgenc@gmail.com

trical, chemical, and optical properties.[11,12] Tungsten oxide also demonstrates high performance in a range of applications, including efficient gas sensors, as well as electrochromic, photochromic, and photoanode materials.[13–16] In addition to the notable light–matter interaction properties of stoichiometric tungsten oxide (WO_3), the increased carrier density caused by oxygen vacancies in sub-stoichiometric tungsten oxide (WO_{3-x}) induces localized surface plasmon resonance (LSPR) in the near-infrared and visible regions.[17,18] The hot electrons generated by LSPR enhance photo-absorption and increase the availability of photogenerated electrons and holes, thereby boosting photocatalytic activity.[19,20]

Supercapacitors, also known as electrochemical capacitors, are energy storage devices that bridge the gap between conventional capacitors and batteries.[21] They are characterized by high power density, rapid charge and discharge rates, and long cycle life, making them ideal for applications requiring quick bursts of energy.[22] Unlike batteries, which rely on chemical reactions, supercapacitors store energy through electrostatic interactions, allowing for faster energy transfer.[23] The performance of supercapacitors depends heavily on the electrode materials, which must have a high surface area, excellent conductivity, and stability.[24] Among various transition metal oxides used as electrode materials, tungsten trioxide (WO_3) has garnered significant attention.[25] Tungsten oxides are promising for supercapacitors due to their natural abundance, high thermal stability, corrosion resistance, multiple valency, and wide negative potential range, as well as their tunnel-like structure that facilitates easy ion insertion of the electrolyte.[26,27] In this context, tungsten oxide (WO_3) and its sub-stoichiometric form (WO_{3-x}) have emerged as strong candidates due to their unique structural and electronic properties.[28] The oxygen vacancies in WO_{3-x} enhance its conductivity and charge storage capacity, making it particularly well-suited for supercapacitor applications.[29] This study investigates the phase-dependent electrochemical properties of WO_3 and WO_{3-x} nanowires, offering insights into their potential for improving supercapacitor performance.

In this study, we synthesized stoichiometric (WO_3) and sub-stoichiometric (WO_{3-x}) tungsten oxide nanowires by controlling their phases and morphologies *via* the hydrothermal method. This work addresses a significant gap in the literature by presenting the properties of one-dimensional WO_3 and WO_{3-x} nanostructures with similar morphological features and phases from a comprehensive perspective. We explore how oxygen vacancies impact photocatalytic, electrochemical, and capacitive performance. By leveraging the complementary properties of these materials in both symmetric and asymmetric configurations, this research seeks to optimize their application in advanced energy storage systems.

2. Experimental section

2.1. Syntheses of phase controlled WO_3 nanowires

All chemicals were of analytical grade and used without further purification.

Synthesis of WO_3 nanowires. 5 mmol of sodium tungstate (Na_2WO_4) powder was dissolved in 50 ml of deionized water at room temperature under vigorous stirring. To this solution, 3 M HCl was added dropwise until the pH reached approximately 1.5. Next, 5 mmol of potassium sulfate (K_2SO_4) was added, and the solution was stirred further for at least 30 minutes at room temperature. The resulting solution was then transferred to a 100 ml Teflon-lined stainless-steel autoclave and heated in an oven at 180 °C for 12 hours. After cooling the autoclave naturally to room temperature, the synthesized products were centrifuged and washed several times with deionized water and ethanol. The precipitates were then dried overnight at 60 °C under vacuum.

Synthesis of WO_{3-x} nanowires. The synthesis of WO_{3-x} nanowires followed the same procedure as described above, except that 5 mmol of sodium sulfate (Na_2SO_4) was added instead of K_2SO_4.

2.2. Materials characterization

Phase analysis of the prepared samples was conducted using a Philips X'Pert Pro X-ray diffractometer (XRD) with Cu-Kα radiation. The microstructural features of the samples were examined with a field emission gun FEI QUANTA 250 scanning electron microscope (SEM). Absorbance spectra for numerical simulations were obtained from solid samples using a Shimadzu UV-3600 UV-Vis-NIR spectrophotometer with diffuse reflectance spectroscopy, and then converted to absorbance using Kubelka–Munk reflectance theory.[30]

2.3. Numerical calculations

The finite difference time domain (FDTD) method was used to investigate the optical properties of stoichiometric (WO_3) and sub-stoichiometric (WO_{3-x}) nanowires. In the simulations, a plane wave was applied, and radii derived from SEM images were used for modeling. Since the synthesized materials consist of one-dimensional nanowires, only the cross-section of each nanowire was considered, disregarding length. The absorption spectrum was modeled using Mie–Gans theory to align with experimental data, as represented by the equation below.[18] This equation incorporates the dielectric properties of the surrounding medium, ε_m, and those of the nanoparticle, including the real (ε_1) and imaginary (ε_2) components, as well as depolarization factors (P_j, where j = 1, 2, 3 for the x, y, and z axes, respectively) across the three dimensions of the nanoparticle. Based on this model, wavelength-dependent dielectric functions and refractive indices were calculated. Additionally, the field distribution was modeled to examine the electric field behavior at the absorption peaks.

$$A \propto \omega {\varepsilon_m}^{3/2} \sum_j \frac{\left(\frac{1}{{P_j}^2}\right)\varepsilon_2}{\left(\varepsilon_1 + \frac{1-P_j}{P_j}\varepsilon_m\right)^2 + {\varepsilon_2}^2} \tag{1}$$

2.4. Photocatalytic activities

The photocatalytic activities of the samples were measured under AM 1.5-filtered simulated solar light using a 500 W xenon lamp. Rhodamine B (RhB) served as a benchmark organic pollutant to evaluate the photocatalytic performance of the tungsten oxide nanowire powders. In a typical experiment, 40 mg of synthesized powder was added to 80 ml of an RhB solution (10 mg RhB per L). The solutions were stirred continuously in the dark for 1 hour to achieve adsorption/desorption equilibrium. At various irradiation intervals, 3 ml aliquots were taken, and the catalyst powders were separated from the solution by centrifugation. The dye concentration, and thus the photocatalytic activity, was measured using UV-Vis spectroscopy (Shimadzu UV-3600 UV-Vis-NIR spectrophotometer). Additional photocatalytic activity tests were performed by adding 0.5 ml of hydrogen peroxide (H_2O_2) to the solution, at approximately pH 2.5 achieved by adding concentrated sulfuric acid, and under conditions with both H_2O_2 and at pH 2.5.

2.5. Electrochemical measurements

The electrochemical performance and characterization of WO_3-based electrode materials, as well as the fabricated symmetric and asymmetric supercapacitor (SC) devices, were conducted using a multi-channel BioLogic VMP 300 potentiostat in a two-electrode configuration. A 6 M KOH aqueous solution was used as the electrolyte to evaluate the electrochemical properties of WO_3-based electrodes. Stainless steel screws served as current collectors on both sides, while porous glass fiber paper (Whatman, grade GF/F) was used as a separator. The synthesized WO_3 powders were used directly as electrodes in both symmetric and asymmetric SC devices without any additional processing, binders, or additives. The details of the symmetric and asymmetric supercapacitor configurations with WO_3 and WO_{3-x} as electrodes are summarized in Table 1, and a schematic of the two-electrode systems is shown in Scheme 1.

All tests were performed at room temperature using cyclic voltammetry (CV), potentiostatic electrochemical impedance

Table 1 Comprehensive details regarding each component of the supercapacitor design

Sample	Electrode (E_1)	Electrode (E_2)	Electrolyte (EI)	Separator (S)	Type
WO_{3-x}	WO_{3-x}	WO_{3-x}	6 M KOH	Glass fiber	Symmetric
WO_3	WO_3	WO_3	6 M KOH	Glass fiber	Symmetric
$WO_{3-x}//WO_3$	WO_{3-x}	WO_3	6 M KOH	Glass fiber	Asymmetric

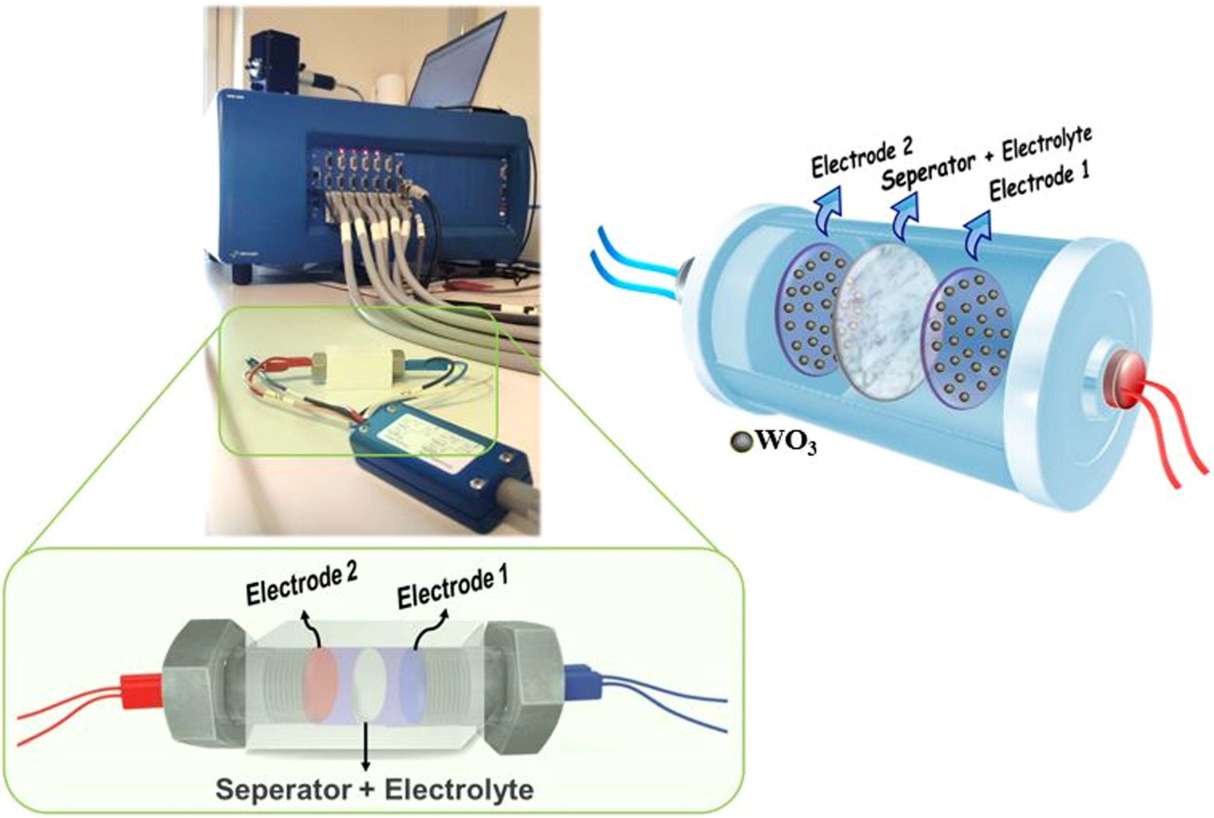

Scheme 1 Schematic representation of the fabricated supercapacitor design.

spectroscopy (PEIS or EIS), and potential-limited galvanostatic cycling (GCPL) techniques. For CV characterization, 20 cycles were recorded at scan rates ranging from 10 to 200 mV s^{-1} within a voltage range of 0 to +1 V. GCPL measurements were conducted for 50 cycles at current densities of 0.1 A g^{-1}, 0.15 A g^{-1}, 0.2 A g^{-1}, 0.3 A g^{-1}, 0.5 A g^{-1}, and 2.4 A g^{-1}.

3. Results and discussion

3.1. Microstructural features

The microstructural features of the samples are presented in Fig. 1. The XRD pattern of the WO_{3-x} nanowires (Fig. 1a) reveals that the sample consists of a monoclinic tungsten oxide phase (JCPDS no. 5-0392, space group: $P2/m$) with lattice parameters of a = 1.828 nm, b = 0.3775 nm, c = 1.398 nm, and β = 115.2°. The peak at $\sim 2\theta = 23°$ corresponds to the (010) plane of the monoclinic phase, indicating a nanowire growth direction along [010].[31] Fig. 1b displays a typical XRD pattern for the WO_3 nanowires, indexed to the hexagonal WO_3 phase (JCPDS no. 33-1387, space group: $P6/mmm$) with lattice parameters of a = 0.7298 nm and c = 0.3899 nm.

SEM images of WO_{3-x} and WO_3 nanowires are shown in Fig. 1c, e and d, f, respectively. These images indicate that both samples exhibit nearly monodispersed one-dimensional nanostructures with typical lengths exceeding 5 μm. The WO_{3-x} nanowires have a thickness of approximately 19 nm, while the WO_3 nanowires are around 210 nm thick. Despite this variation in thickness, both nanowire types share the same overall morphology, where the thicker WO_3 nanowires are also formed by thinner building blocks (Fig. 1f) However, the distinct phases make them ideal candidates for studying phase-dependent properties, particularly the influence of oxygen vacancies, across various applications.

3.2. Optical properties and FDTD simulations

The UV-Vis absorption spectra of WO_{3-x} (black) and WO_3 (red) nanowires are shown in Fig. 2a. These spectra were derived from diffuse reflectance measurements of the solid powders using Kubelka–Munk reflectance theory.[30] The prominent absorption peaks appear at approximately 284 eV for WO_{3-x} nanowires and 286 eV for WO_3 nanowires, with shoulder peaks at ∼242 eV for WO_{3-x} and ∼244 eV for WO_3 nanowires. Notably, the WO_{3-x} nanowires exhibit significantly higher light absorbance in the UV and NIR regions compared to the WO_3 nanowires. This enhanced NIR absorption in WO_{3-x} nanowires is likely related to the presence of localized surface plasmon resonances.[18] To determine the optical band gap values of the nanowires, Tauc plots were created,[32,33] as shown in Fig. 2b and c for WO_{3-x} and WO_3 nanowires, respectively. These plots indicate that the optical band gaps are calculated as 2.98 eV for WO_{3-x} nanowires and 3.22 eV for WO_3 nanowires. Surface energies, defect sites, and electronic band structures of various tungsten oxide phases with different atomic coordination are studied in the literature.[34] The amounts and energy values of oxygen vacancies in different sub-stoichiometric tungsten oxide structures have been reported by using different techniques such as X-ray photoelectron spectroscopy (XPS), electron paramagnetic resonance (EPR) spectroscopy and density functional theory (DFT)-based simulations.[35–37] Most of these studies consider the effect of low-density oxygen vacancies on the properties of tungsten oxide, however, as seen in Fig. 1, here we report tungsten oxide phases with different crystal structures where the oxygen-vacancies are high enough to change the full crystal structure of the nanowires.

The real and imaginary parts of the dielectric functions and refractive indices were calculated from the data obtained from the normalized absorption spectra shown in Fig. 2 by substituting the wavelength-dependent dielectric functions into eqn (2), as shown below and illustrated in Fig. 3:

$$n_{\lambda}{}^{2} = n + \mathrm{i}\kappa = \varepsilon_1 + \mathrm{i}\varepsilon_2 \tag{2}$$

The dielectric function of a material has two components: the real part, which relates to energy storage and the polarization of the material, and the imaginary part, which represents energy absorption and loss. Fig. 3a shows the real (solid lines) and imaginary (dashed lines) parts of the dielectric functions for WO_{3-x} and WO_3 nanowires. A comparison of these graphs reveals that WO_{3-x} nanowires demonstrate superior energy storage, transfer, and light absorption capabilities compared to WO_3 nanowires, consistent with the absorption spectra in Fig. 2a.

Fig. 3b displays the real and imaginary parts of the refractive indices for WO_{3-x} and WO_3 nanowires. The real part of the refractive index indicates the speed of light within the material, while the imaginary part reflects the extinction coefficient, which is related to light absorption. As shown by the imaginary parts in Fig. 3b, WO_{3-x} nanowires exhibit higher light absorption at a given wavelength than stoichiometric WO_3 nanowires.

Fig. 4 illustrates the field distribution around tungsten oxide nanowires at their respective maximum absorption wavelengths. As shown, the 19 nm thick WO_{3-x} nanowire exhibits a strong dipolar field distribution (Fig. 4a), while the 210 nm thick WO_3 nanowire displays a multipolar mode. The field intensity around the WO_{3-x} nanowire is approximately 32% stronger than that around the WO_3 nanowire.

3.3. Photocatalytic activities

Oxygen vacancies in metal oxides can serve as adsorption and active sites, significantly enhancing the efficiency of photocatalytic reactions by increasing light absorption, charge separation, and surface reactivity in these materials.[38] Charge separation associated with oxygen vacancies in metal oxides leads to the formation of unpaired electrons, which can potentially create donor levels within the material.[39,40]

Fig. 5 shows the photocatalytic activities of the WO_{3-x} nanowires (Fig. 5a) and the WO_3 nanowires (Fig. 5b) for the degradation of RhB dye under AM 1.5 filtered simulated solar light. The photodegradation ratios of both samples *versus* irradiation

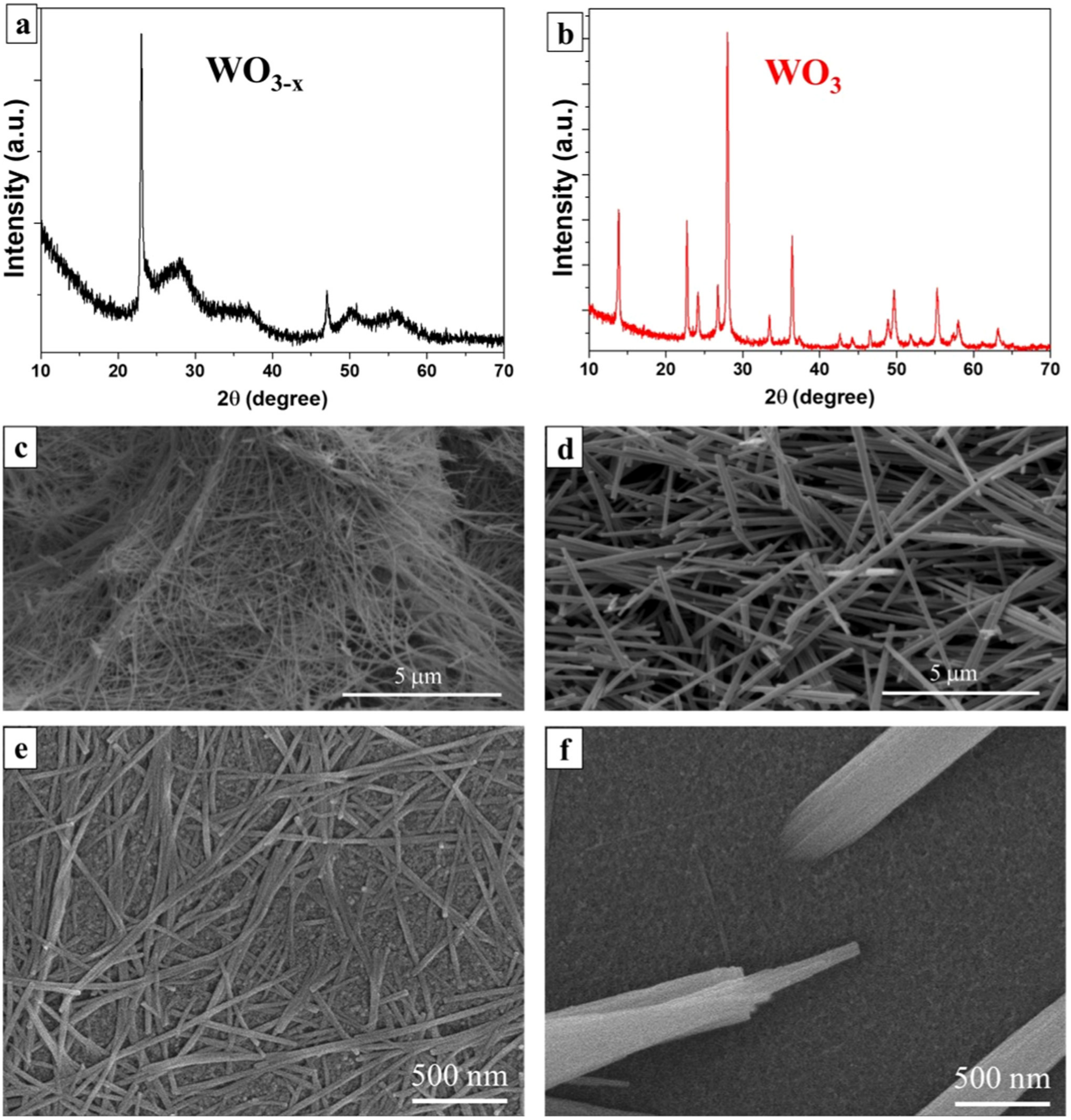

Fig. 1 Microstructural features of the samples: (a) XRD pattern of WO_{3-x} nanowires, (b) XRD pattern of WO_3 nanowires, (c) and (e) SEM image of WO_{3-x} nanowires, and (d) and (f) SEM image of WO_3 nanowires.

times are shown in Fig. 5c, which also includes the photolysis of RhB (degradation under simulated solar light without any catalyst) under the same illumination conditions. As detailed in the Experimental section, 40 mg of tungsten oxide nanowires were added to 80 ml of RhB solution (10 mg RhB per L), and the solutions were mixed using continuous magnetic stirring in the dark for 1 hour to achieve adsorption/desorption equilibrium.

RhB is one of the most studied compounds in photocatalytic dye degradation studies, where reactive oxygen species (ROS) play a crucial role in degrading organic pollutants through heterogeneous photocatalysis. In the heterogeneous photocatalytic process, electrons (e^-) in the conduction band (CB) and holes (h^+) in the valence band (VB) are generated within the photoactive semiconductor upon illumination. ROS, such as singlet oxygen ($^1O_2$), superoxide anion

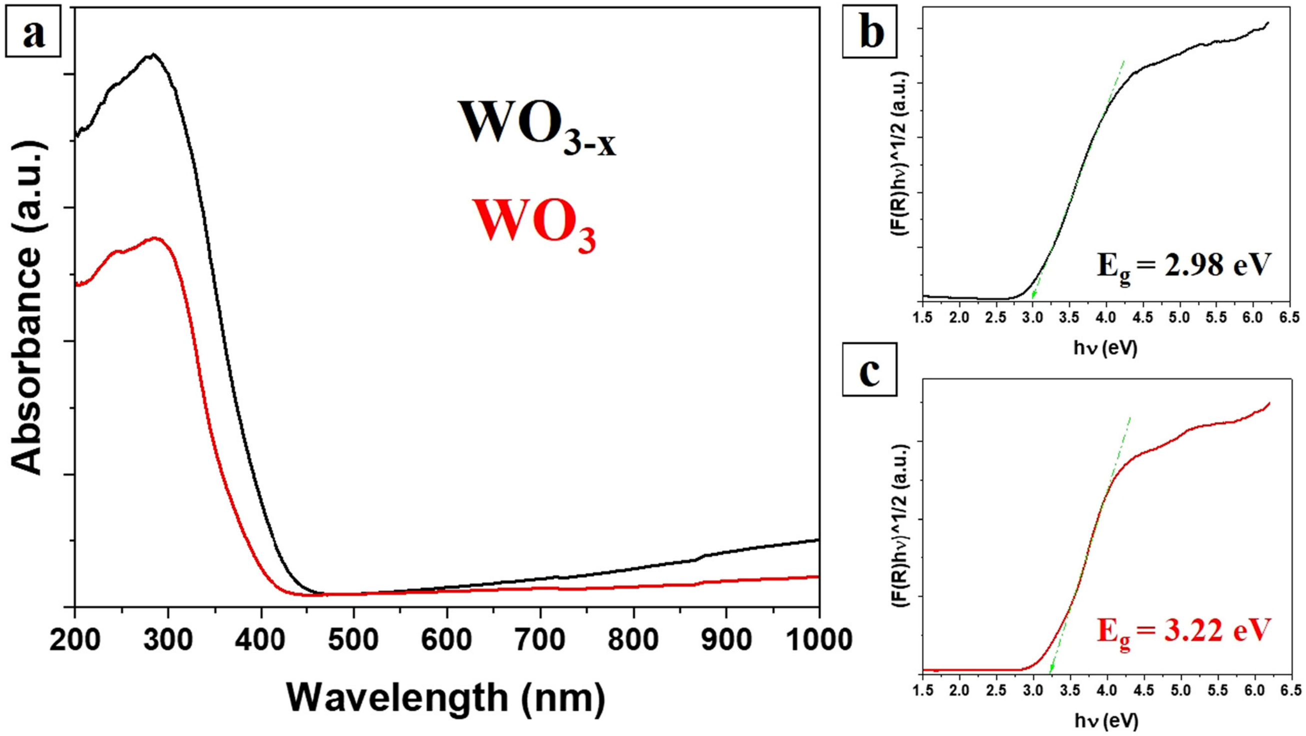

Fig. 2 (a) UV-Vis absorption spectra of the WO_{3-x} (in black) and WO_3 (in red) nanowires. (b) and (c) are Tauc's plots used to determine the optical band gap for the WO_{3-x} and WO_3 nanowires, respectively.

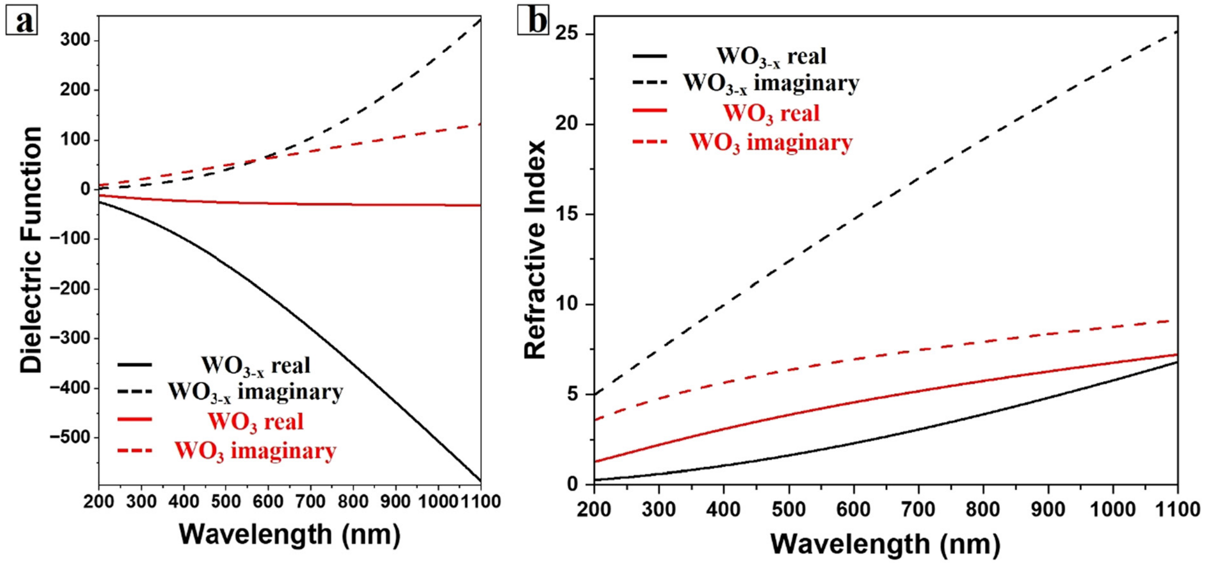

Fig. 3 (a) Real (solid lines) and imaginary (dashed lines) parts of the dielectric function of the WO_{3-x} nanowires (in black) and WO_3 nanowires (in red), derived from absorption data fitted using the Mie formula. (b) Real (solid lines) and imaginary (dashed lines) parts of the refractive index of the WO_{3-x} nanowires (in black) and WO_3 nanowires (in red), also derived from absorption data fitted with the Mie formula.

radical ($^•O_2^-$), hydrogen peroxide (H_2O_2), and hydroxyl radical ($^•OH$), are produced through reactions between photoinduced holes and electrons in the aquatic medium.[41] It is well known that these highly reactive and non-selective ROS effectively attack the chemical bonds of organic molecules, facilitating their degradation into harmless byproducts such as carbon dioxide and water.[42] The stepwise mechanisms are represented below:[43]

$$h\upsilon \rightarrow e^- + h^+$$

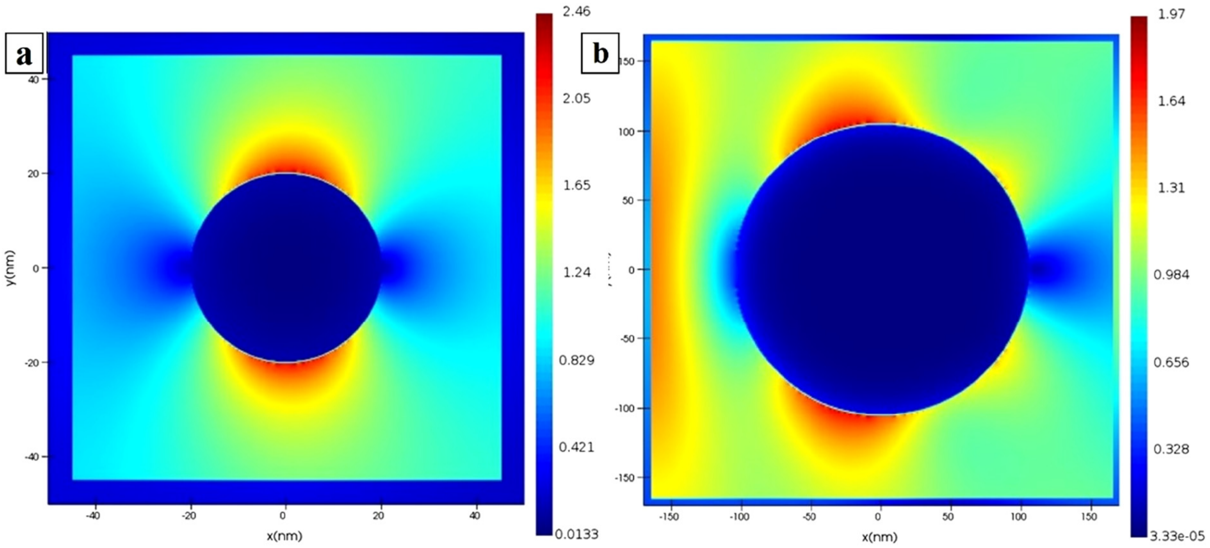

Fig. 4 (a) Field distribution around the WO_{3-x} nanowires at the maximum absorption peak of 284 nm. (b) Field distribution around the WO_3 nanowires at the maximum absorption peak of 286 nm.

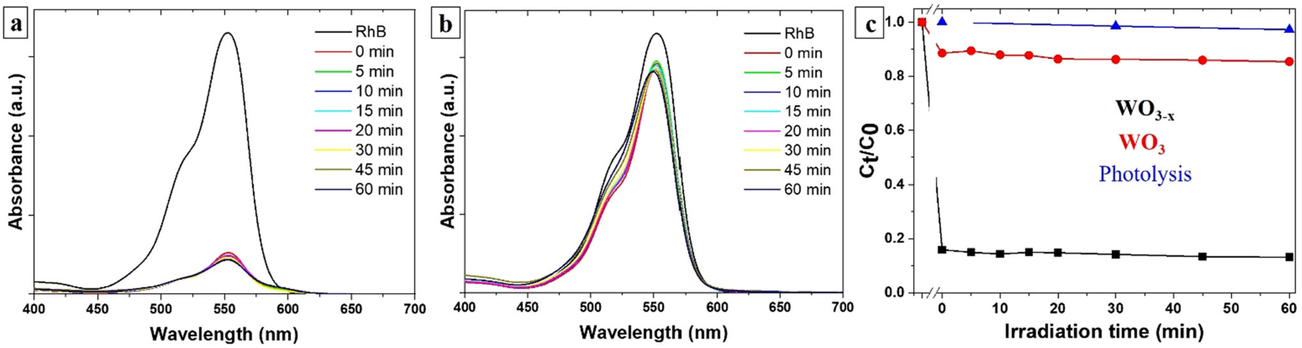

Fig. 5 (a) UV-Vis absorption spectra of RhB solutions containing the WO_{3-x} nanowires as photocatalysts after various solar irradiation times. (b) UV-Vis absorption spectra of RhB solutions containing the WO_3 nanowires as photocatalysts after different solar irradiation times. (c) Photodegradation ratio *vs.* irradiation times for both samples, along with the photolysis of RhB (without any catalyst). The photodegradation ratio in (c) is calculated using the Beer–Lambert law at the indicated time intervals, where C_0 represents the initial concentration of RhB and C_t represents the concentration of RhB at the specified irradiation times.

$$h^+ + H_2O\ (ads) \rightarrow HO^{\bullet}\ (ads) + H^+\ (ads)$$

$$O_2 + 2e^- \rightarrow O_2^{\bullet -}(ads)$$

$$O_2^{\bullet -}(ads) + H^+ \leftrightarrow HO^{\bullet}_2\ (ads)$$

$$HO^{\bullet}_2\ (ads) \rightarrow H_2O_2\ (ads) + O_2$$

$$H_2O_2\ (ads) \rightarrow 2HO^{\bullet}\ (ads)$$

$$HO^{\bullet} + dye \rightarrow intermediates \rightarrow CO_2 + H_2O$$

As seen in Fig. 5a and c, the WO_{3-x} nanowires adsorb a substantial amount (~84.1%) of RhB after mixing in the dark for 1 hour. The remaining RhB in the solution is reduced to 15% after 5 minutes of light irradiation, decreasing further to ~13% after 60 minutes. These results demonstrate that the WO_{3-x} nanowires are highly effective adsorbents for RhB under ambient conditions and their photocatalytic performances couldn't be assessed reliable with such a high ratio of adsorbed RhB. It may be assumed that, since the majority of the RhB is adsorbed on the surface of the WO_{3-x} nanowires, some of the adsorbed RhB is released back into the solution with prolonged light irradiation, suggesting that the adsorption/desorption and photocatalytic degradation mechanisms occur simultaneously. In contrast, the adsorption of RhB on the WO_3 nanowires is only about 11.5% (Fig. 5b and c), and these nanowires are much less effective for the photocatalytic degradation of RhB, with only 13.7% of the RhB eliminated after 30 minutes of light irradiation. This limited effectiveness can be attributed to the band edge positions of WO_3 in water, which do not align well with the redox potentials for water photolysis, resulting in a weaker reduction potential in the conduction band.[44] A similar behavior has been observed for Fe_2O_3, which has nearly identical band edge positions to WO_3. This issue can be mitigated by adding H_2O_2 to the solution, which acts as an electron acceptor and enhances the photocatalytic reaction.[45]

Such a significant difference in photocatalytic activities, *i.e.* being active and not active, of two different tungsten oxide nanowires are cannot be explained by the thickness differences but can be discussed by taking the above-presented optical properties and band-positions into account. There are certainly other properties that affect the optical properties and photocatalytic activities of tungsten oxide nanostructures. Qasrawi *et al.*[46] reported key optical properties of WO_3 thin films, including their light absorption coefficients and the diffusion paths of charge carriers (holes and electrons), where they emphasized that the absorption coefficient increases as the incident photon energy decreases, primarily due to free carrier absorption mechanisms influenced by phonon scattering. Kalanur *et al.*[47] mention that the theoretical maximum conversion efficiency of tungsten trioxide is approximately 6.3% for photons with energies exceeding 2.6 eV. This highlights WO_3's ability to absorb light effectively, which is essential for photocatalytic applications. Moreover, they have reported that WO_3 has a hole diffusion length of approximately 150 nm. Accordingly, studies show a correlation between band gap variations and visible light absorption, which directly affects the diffusion paths of holes and electrons in WO_3 particles.[48] These studies emphasize the critical role of surface properties, such as crystallite size and specific surface area, in achieving effective advanced oxidation processes (AOPs).

Additionally, they highlight that the number of active sites is crucial for facilitating redox reactions on the photocatalytic surface.[49,50] For instance, J. Liu *et al.*[51] reported the aspect ratio-dependent photocatalytic activity of ultrathin tungsten oxide nanowires on the degradation of RhB and concluded that the highest aspect ratio nanowires having the highest activity can be related to their higher density of oxygen surface defects along with their higher adsorption capacity. Thus, many factors, such as vacancies acting as active sites for charge carriers and the separation and transfer of electrons and holes generated during photocatalysis, play crucial roles in the performance of a photocatalytic process in addition to the size effects. A thinner morphology may seem more suitable for charge carrier diffusion to the surface, it is not the sole determining factor for photocatalytic performance. The results shown here highlights the importance of taking combined influence of multiple factors into account that rather than attributing the performance of a photocatalytic process to a single phenomenon.

Fig. 6 shows the photocatalytic activities of the WO_{3-x} nanowires (Fig. 6a) and WO_3 nanowires (Fig. 6b) for the degradation of RhB, with the addition of 0.5 ml H_2O_2 to each solution. Compared to the previous results, it is evident that the addition of 0.5 ml H_2O_2 to the solution significantly altered the adsorption behavior of RhB on the surface of the WO_{3-x} nanowires, which is found to be approximately 9.2% with the inclusion of H_2O_2. After 5 and 10 minutes of light irradiation, the remaining RhB in the solution is 17.6% and 16.1%, respectively. A release of adsorbed RhB is observed after 15 minutes, where 24.5% of the dye remains in the solution, and this decreases to 16.5% after 20 minutes, with the photodegradation stabilizing at this level over longer irradiation times. In contrast, as shown in Fig. 6b and c, the WO_3 nanowires efficiently and systematically degrade RhB when 0.5 ml H_2O_2 is added. After approximately 11.2% adsorption in the dark, 50.7% of the RhB is degraded by the WO_3 nanowires within 10 minutes, increasing to 78.5% after 20 minutes of light irradiation. The remaining RhB amount is 14.5% after 30 minutes and decreases systematically with increasing irradiation durations, reaching 9.7% after 60 minutes. As seen in these figures, the photocatalytic activity of both samples decreases with prolonged irradiation. Along with the fact that the amount of RhB being lower in the environment, such a loss in photoactivity of tungsten oxide, especially for the WO_{3-x} nanowires, can be attributed to a complex photo-corrosion process, as explained by Seabold and Choi.[52] This process involves the formation of peroxo species at the WO_3 surface,[52,53] which can result from the oxidation of surface

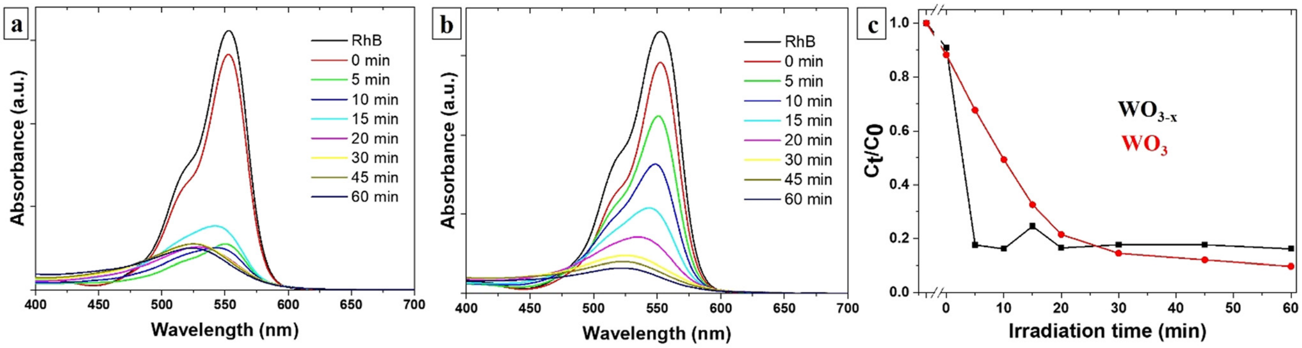

Fig. 6 (a) UV-Vis absorption spectra of RhB solutions containing 0.5 ml H_2O_2 and WO_{3-x} nanowires as photocatalysts after different solar irradiation times. (b) UV-Vis absorption spectra of RhB solutions containing 0.5 ml H_2O_2 and WO_3 nanowires as photocatalysts after different solar irradiation times. (c) Photodegradation ratio *vs.* irradiation time for both samples.

hydroxyl groups or the adsorption of hydroxyl radicals or peroxides.[54] The direct addition of hydrogen peroxide to the solution accelerates the formation of these species, leading to a decrease in the overall photoactivity.

Adding H_2O_2 to the system significantly increased the photocatalytic activity of the WO_3 nanowires and drastically changed the adsorption behavior of RhB on the WO_{3-x} nanowires. To investigate such alternating behaviors further, we explored the effect of pH, specifically lowering the pH to inhibit the formation of peroxo species on the surface of the photocatalysts. It has been reported that WO_3 is chemically stable in strongly acidic solutions but undergoes severe corrosion due to OH^--induced dissolution in solutions with pH > 4.[55] Due to above-mentioned photo-corrosion mechanism resulting the formation of hydrogen peroxide in solution, generated by the photocatalytic reaction, along with the accumulation of a peroxo species layer on the WO_3 surface, photocatalytic activities of the WO_3 photocatalyst can be limited. It has been reported that lower pH conditions suppress peroxide formation on the WO_3 photocatalyst surface.[56] The pH of the RhB solution was lowered to ~2.5 by adding concentrated sulfuric acid, and the photocatalytic activity tests were repeated.

Fig. 7 shows the photocatalytic activities of the WO_{3-x} nanowires (Fig. 7a) and WO_3 nanowires (Fig. 7b) for the degradation of RhB at a pH of 2.5. The performance of the WO_{3-x} nanowires is similar to that observed under neutral conditions (Fig. 5a), with RhB adsorption measured at ~45.6%. After 10 minutes of light irradiation, the remaining RhB concentration is approximately 10%. As the irradiation continues, some adsorbed RhB is released, and the remaining RhB after 60 minutes is about 11.9%. The WO_3 nanowires, which showed minimal activity without H_2O_2, behave similarly to the neutral conditions when the pH is adjusted to 2.5. After 30 minutes of light irradiation, only 12.9% of the RhB was removed from the solution, confirming their limited photocatalytic performance under these acidic conditions. Along with the lower pH conditions, studies suggest that the photostability and photoactivity of WO_3 can be enhanced through the controlled introduction of oxygen vacancies, as sub-stoichiometric WO_{3-x} exhibits high resistance to re-oxidation and peroxo species-induced dissolution.[57]

To further investigate the impact of H_2O_2 at low pH, we repeated the photocatalytic tests for the RhB solutions at pH 2.5, which also contained 0.5 ml of H_2O_2. The results are shown in Fig. 8. As seen in Fig. 8a, corroborating with the

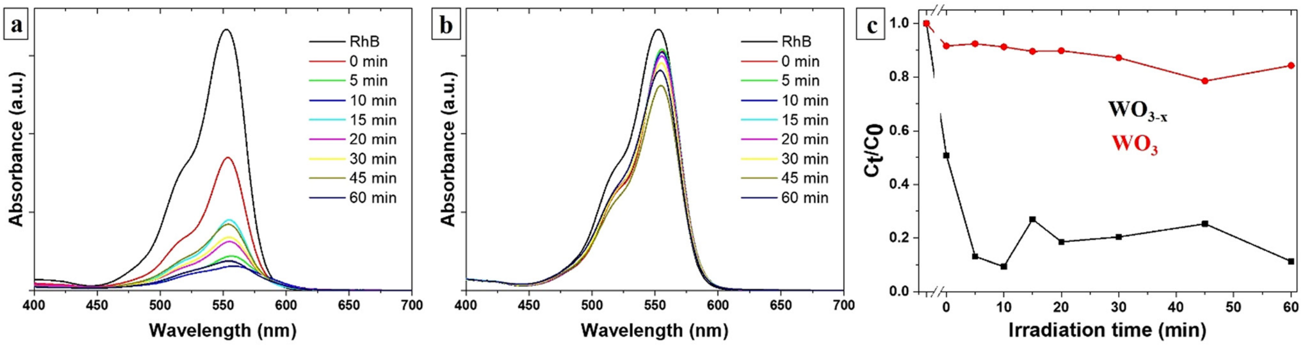

Fig. 7 (a) UV-Vis absorption spectra of RhB solutions at a pH of 2.5, containing the WO_{3-x} nanowires as photocatalysts after different solar irradiation times. (b) UV-Vis absorption spectra of RhB solutions at a pH of 2.5, containing the WO_3 nanowires as photocatalysts after different solar irradiation times. (c) Photodegradation ratio *vs*. irradiation times for both samples.

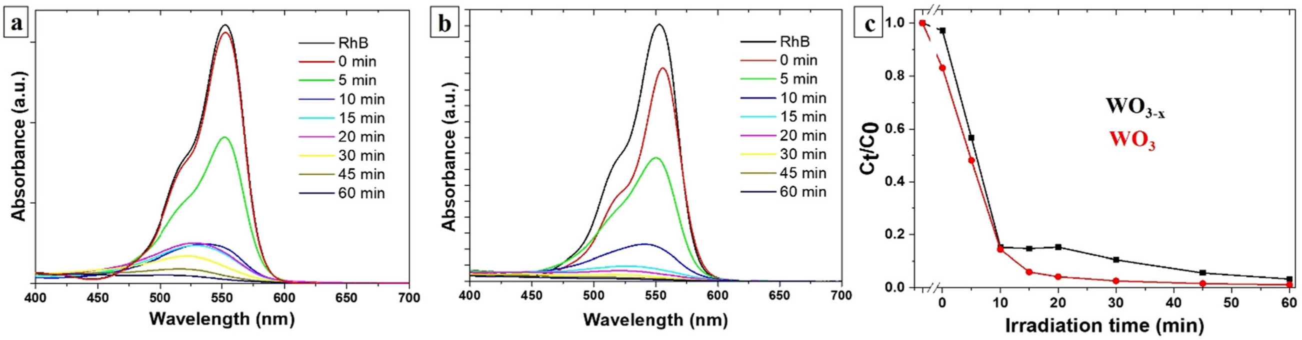

Fig. 8 (a) UV-Vis absorption spectra of RhB solutions at a pH of 2.5, containing 0.5 ml H_2O_2 and the WO_{3-x} nanowires as photocatalysts after different solar irradiation times. (b) UV-Vis absorption spectra of RhB solutions at a pH of 2.5, containing 0.5 ml H_2O_2 and the WO_3 nanowires as photocatalysts after different solar irradiation times. (c) Photodegradation ratio *vs*. irradiation times for both samples.

results presented in Fig. 6, the adsorption of RhB on the surface of the WO_{3-x} nanowires is almost negligible amount of 2.9% after 1 hour of mixing in the dark with the presence of H_2O_2 at low pH. A significant amount of the remaining RhB is degraded after 5 minutes of light irradiation, reducing the RhB concentration in the solution to approximately 56.6%, which is further decreased to 15.2% after 10 minutes of light irradiation. After this point, the amount of RhB in the solution almost systematically decreased, reaching 3.3% after 60 minutes of light irradiation. It is shown that the WO_{3-x} nanowires are highly active photocatalysts in these conditions (0.5 ml H_2O_2 at pH = 2.5). Similarly, the WO_3 nanowires are also highly effective photocatalysts in these conditions, performing even better than the WO_{3-x} nanowires. The adsorption of RhB on the surface of the WO_3 nanowires was around 17%. After 5 minutes of light irradiation, approximately 51.9% of the RhB was degraded, with the remaining concentration dropping to 14.3% after 10 minutes and to 5.9% after 15 minutes. After 60 minutes of irradiation, 99% of the RhB was degraded. The significant improvement in photocatalytic activity with the addition of H_2O_2 and the low pH is clearly observed when comparing the results presented in Fig. 6 and

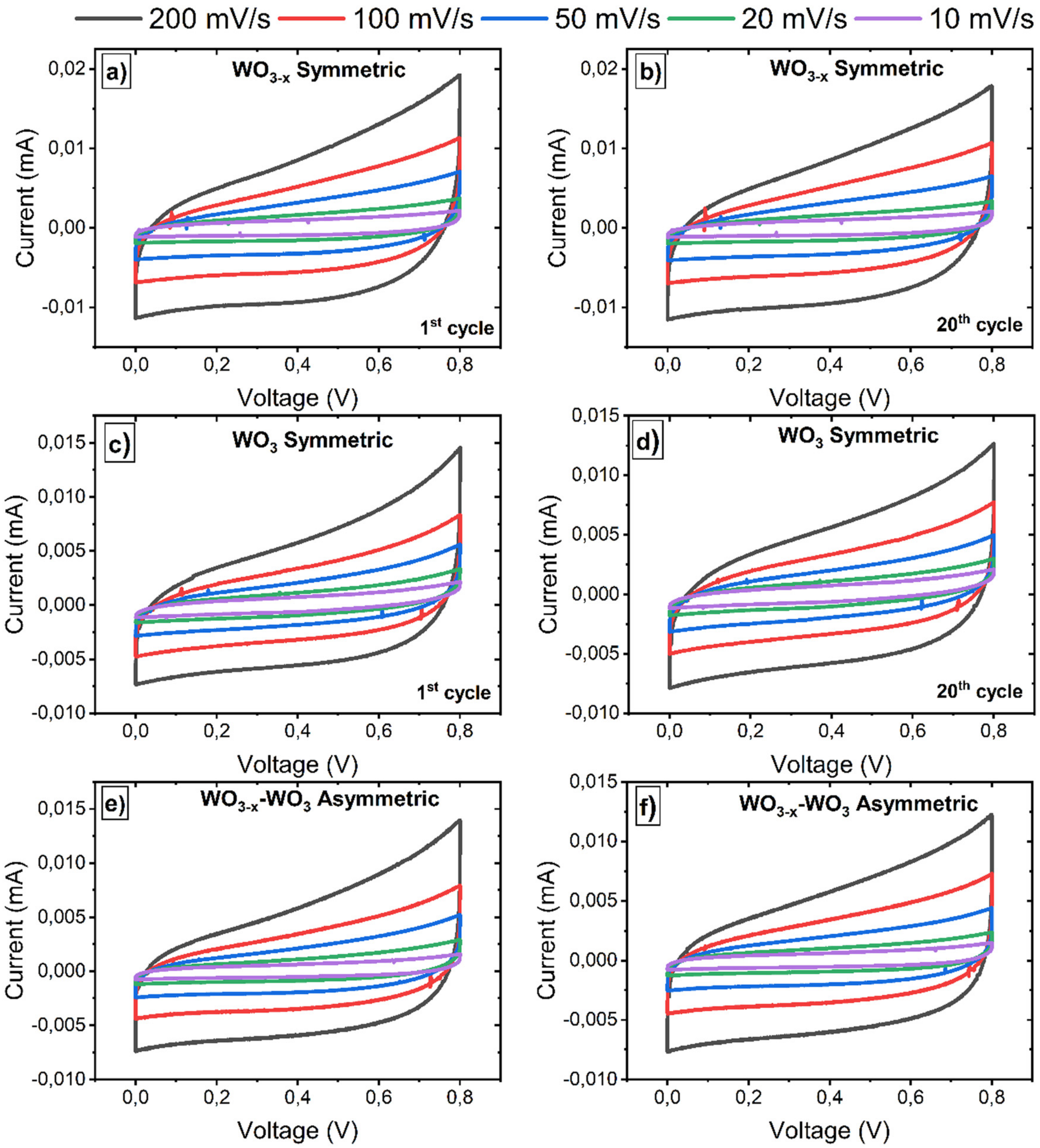

Fig. 9 CV curves of WO_{3-x} and WO_3 nanowires in symmetric and asymmetric configurations at various scan rates. (a) and (b) show the first and twentieth cycles for WO_{3-x} symmetric, respectively; (c) and (d) display the first and twentieth cycles for WO_3 symmetric; (e) and (f) illustrate the first and twentieth cycles for the $WO_{3-x}//WO_3$ asymmetric configuration.

8. Unlike under neutral conditions, the photocatalytic activity does not stagnate at pH 2.5, which is crucial for continuous photoactivity (Fig. 9).

3.4. Electrochemical properties and supercapacitor performance test

For electrochemical measurements and supercapacitor performance tests, symmetrical devices (WO_{3-x} and WO_{3-x}) (WO_3 and WO_3) with both electrodes made of the same material, and asymmetric devices with different electrodes were designed (WO_{3-x} and WO_3).

The CV results can be related to other analyses in the manuscript, such as the structural and optical properties of WO_3 and WO_{3-x} nanowires. The enhanced electrochemical performance of WO_{3-x}, as seen in the CV curves, is consistent with its structural features, including the presence of oxygen vacancies. These vacancies, identified in the microstructural analysis, contribute to increased conductivity and active sites for charge storage, which are reflected in the higher current densities observed in the CV results. The optical properties, particularly the UV-Vis absorption spectra, also support the CV findings. As discussed in the optical analysis, the increased light absorption and localized surface plasmon resonances in WO_{3-x} correlate with its superior electrochemical behavior. This enhanced light absorption likely contributes to the improved charge transfer processes observed in the CV analysis. In the asymmetric design (WO_{3-x}//WO_3), the broader potential window and higher capacitance observed in the CV curves can be linked to the complementary properties of the two materials. The structural and optical analyses suggest that WO_{3-x} provides high capacitance due to its vacancies, while WO_3 offers stability, allowing for efficient charge transfer and storage. This synergy is evident in the improved performance of the asymmetric supercapacitor design. The obtained CV results are in harmony with the structural and optical analyses, highlighting the advantages of WO_{3-x} in enhanced electrochemical performance and the effective combination of WO_3 and WO_{3-x} in asymmetric configurations. Impedance spectroscopy is an essential technique for evaluating the electrochemical properties of materials, providing insights into charge transfer resistance,[58] capacitance, and other critical parameters.[59] In our study, the impedance results are intricately linked to the structural and optical analyses of WO_3 and WO_{3-x} nanowires. Oxygen vacancies in WO_{3-x} significantly enhance its conduc-

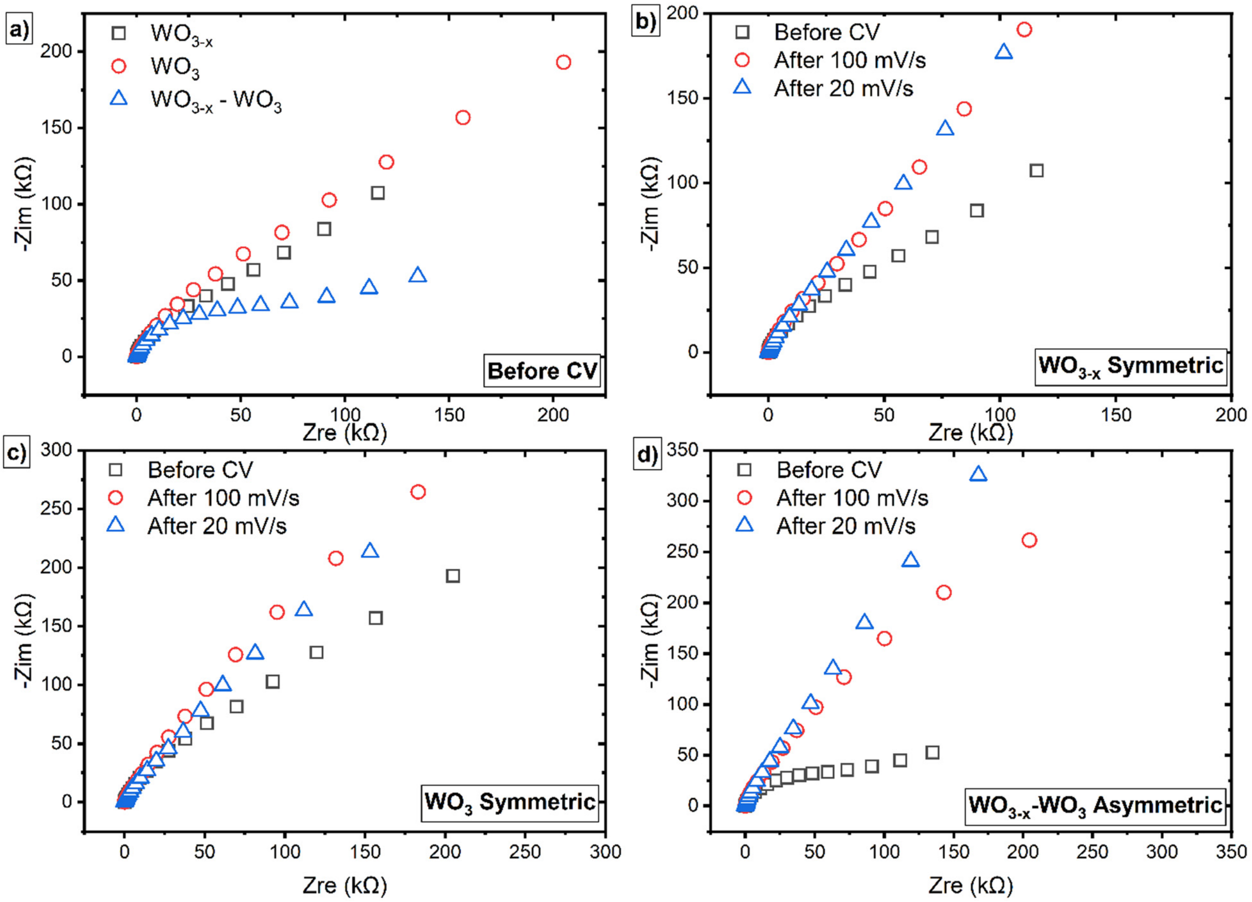

Fig. 10 Nyquist plots from impedance spectroscopy of WO_{3-x} and WO_3 nanowires in symmetric and asymmetric configurations. (a) Before CV analysis, (b) WO_{3-x} symmetric configuration, (c) WO_3 symmetric configuration, and (d) WO_{3-x}//WO_3 asymmetric configuration. The plots illustrate the impedance behavior before CV and after CV at 100 mV s^{-1} and 20 mV s^{-1}, highlighting the changes in charge transfer resistance and capacitance.

tivity by facilitating electron mobility and reducing charge transfer resistance.[60] This is evident in the impedance spectra, where WO_{3-x} consistently shows lower resistance than WO_3, underscoring its superior electrochemical performance. In the asymmetric design (WO_{3-x}//WO_3), the impedance spectra reveal a synergistic combination of the properties of both materials. The lower resistance and higher capacitance observed in this setup are due to the complementary electrochemical characteristics of WO_3 and WO_{3-x}. WO_{3-x} contributes high conductivity and active sites for charge storage, while WO_3 provides structural stability, allowing for efficient charge transfer and storage. This synergy is reflected in the enhanced performance of the supercapacitor, as demonstrated by the broader potential window and improved capacitance. The impedance analysis before and after CV further illustrates the dynamic adaptability of these materials. Initially, the impedance is higher, indicating some resistance. However, after CV, particularly at 100 mV s^{-1} and 20 mV s^{-1}, the impedance decreases, suggesting improved charge transfer and reduced resistance due to the activation of the electrode materials during cycling. This change highlights the materials' ability to adapt to electrochemical processes, aligning with the enhanced performance observed in the CV analysis. When integrated with the structural and optical analyses, the impedance results emphasize the advantages of WO_{3-x} in terms of enhanced electrochemical performance and the effective combination of WO_3 and WO_{3-x} in asymmetric configurations. GCPL analysis is a technique used to evaluate electrode materials' charge storage capacity and stability by applying a constant current and measuring the resulting voltage changes over multiple cycles (Fig. 10).[61,62]

Our study's GCPL results are intricately linked to the structural, optical, and electrochemical analyses of WO_3 and WO_{3-x} nanowires. The structural analysis, including XRD and SEM, revealed that WO_{3-x} nanowires possess thinner nanowires and a higher density of oxygen vacancies than WO_3. These features contribute to their enhanced electrochemical performance by providing a more active sites for charge storage. The GCPL results align with the CV and impedance spectroscopy findings, which showed enhanced electrochemical performance for WO_{3-x} due to its structural and compositional features. The increased specific capacitance observed in WO_{3-x} is consistent with its higher current densities and lower charge transfer resistance identified in CV and impedance analyses. Oxygen vacancies in WO_{3-x} also enhance electron mobility and conductivity, further supporting the superior performance observed in GCPL. Optical properties, such as UV-Vis absorption, also corroborate these findings, as WO_{3-x} demonstrates improved light absorption, which can enhance charge transfer processes and contribute to its superior electrochemical behavior.[63] This improved light absorption indicates the material's ability to interact with a broader light spectrum, potentially facilitating additional charge generation and transfer. In the asymmetric design (WO_{3-x}//WO_3), the GCPL results show improved specific capacitance and stability compared to symmetric designs. This is due to the complementary properties of WO_3 and WO_{3-x}, where WO_{3-x} offers high capacitance, and WO_3 provides structural strength. This combination allows for efficient charge transfer and storage, enhancing the overall performance of the supercapacitor. The GCPL findings are consistent with the CV and impedance analyses, which also demonstrated the superior performance of WO_{3-x} and the

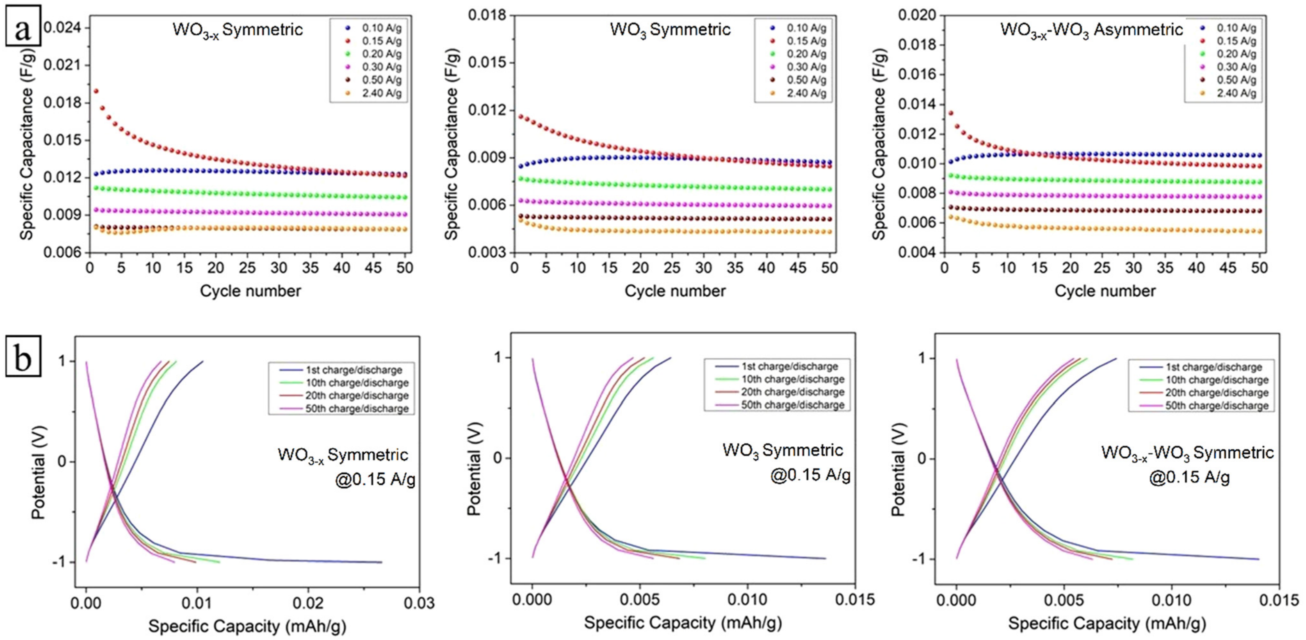

Fig. 11 GCPL analysis of WO_3 and WO_{3-x} nanowires. (a) Specific capacitance changes at various current densities after 50 cycles for each design, (b) specific capacity (mA h g^{-1}) values after 1, 10, 20, and 50 charge/discharge cycles.

effective synergy in the asymmetric design. The enhanced charge storage and stability observed in GCPL further validate the advantages of using WO_{3-x} in energy storage applications. WO_{3-x} and WO_3 as electrodes in symmetric and asymmetric designs offer distinct advantages in electrochemical applications. WO_{3-x}, with its higher density of oxygen vacancies, provides enhanced conductivity and increased active sites for charge storage, resulting in superior specific capacitance and charge retention. This makes WO_{3-x} particularly effective in symmetric configurations, where its structural features lead to improved electrochemical performance. In asymmetric designs, the combination of WO_{3-x} and WO_3 leverages the high capacitance of WO_{3-x} with the structural stability of WO_3, allowing for efficient charge transfer and storage. This synergy enhances the overall performance of the supercapacitor, as demonstrated by the broader potential window and improved stability observed in the electrochemical analyses. The comprehensive characterization, including CV, impedance spectroscopy, and GCPL tests, underscores the potential of these materials for advanced energy storage applications, optimizing the strengths of both WO_{3-x} and WO_3 (Fig. 11).

4. Conclusions

In this study, we synthesized WO_3 and WO_{3-x} nanowires by controlling their phases and morphologies using the hydrothermal method. By doing so, we were able to systematically investigate the effects of different phases/oxygen vacancies on the optical properties and photocatalytic and supercapacitance applications of these tungsten oxide nanowires.

Optical band gaps for the WO_{3-x} and WO_3 nanowires were found to be 2.98 eV and 3.22 eV, respectively. FDTD simulations revealed that, in corroboration with the experimental absorbance spectra, the WO_{3-x} nanowires are better at storing and sending energy as well as the absorption of light than the WO_3 nanowires. It is also shown by FDTD that the 19 nm thick WO_{3-x} nanowire has a strong dipolar distribution around the nanowires, whereas the field distribution around the 210 nm thick WO_3 nanowire has a multipolar mode where the field intensity around the WO_{3-x} nanowire is about 32% stronger than the WO_3 nanowire.

Photodegradation of RhB was chosen as a benchmark for photocatalytic activity and reveal that the oxygen vacancies have a significant impact on the photocatalytic behavior at different experimental conditions. WO_{3-x} nanowires removed a substantial amount of the RhB, mostly by adsorption, under ambient conditions where the WO_3 nanowires can be considered mostly inactive due to the band edge positions of the WO_3 in water which do not coincide with the redox potentials for water photolysis. Addition of H_2O_2 makes WO_3 nanowires active photocatalysts. Addition of H_2O_2 also changed the surface adsorption behavior of RhB on the WO_{3-x} nanowires. Similar to the neutral conditions, WO_{3-x} nanowires removed a substantial amount of the RhB in 10 min at pH = 2.5, whereas the WO_3 nanowires were mostly inactive. Both nanowires performed a lot better when the solutions were containing H_2O_2 at a pH of 2.5.

For electrochemical measurements and supercapacitor performance tests, symmetrical devices (WO_{3-x} and WO_{3-x}) (WO_3 and WO_3) with both electrodes made of the same material, and asymmetric devices with different electrodes were designed (WO_{3-x} and WO_3). The CV curves revealed an enhanced electrochemical performance for the WO_{3-x} nanowires, which is consistent with the reported microstructural and optical properties where the enhanced light absorption likely contributes to the improved charge transfer processes observed in the CV analyses. The structural and optical analyses suggest that WO_{3-x} nanowires provides high capacitance due to its vacancies, while WO_3 nanowires offers stability, allowing for efficient charge transfer and storage. This synergy is evident in the improved performance of the asymmetric supercapacitor design, where broader potential window and higher capacitance are observed.

Author contributions

Z. Kahraman: conceptualization, formal analysis, investigation, methodology, visualization, writing – original draft; A. Güngör: investigation, methodology, visualization, writing – original draft; M. Buldu-Aktürk: investigation, methodology, visualization, writing – review & editing; M. Tan; investigation, methodology, visualization, writing – review & editing; E. Alp: conceptualization, formal analysis, investigation, methodology, supervision, visualization, writing – original draft; E. Erdem: conceptualization, formal analysis, investigation, methodology, supervision, visualization, writing – original draft; A. Genç: conceptualization, investigation, methodology, project administration, supervision, visualization, writing – original draft.

Data availability

All data leading to the results presented in this article will be made available upon request.

Conflicts of interest

There are no conflicts to declare.

Acknowledgements

Some equipment used in this study is funded by the financial support of the Scientific and Technological Research Council of Turkey (TUBITAK) under project number 121M115, and it is greatly acknowledged. Z. K. acknowledges the funding from TUBITAK BIDED-2218 under the project number 123C456.

References

1 N. L. Panwar, S. C. Kaushik and S. Kothari, *Renewable Sustainable Energy Rev.*, 2011, **15**, 1513–1524.

2 A. Fujishima and K. Honda, *Nature*, 1972, **238**, 37–38.

3 R. M. Hoffmann, S. T. Martin, W. Choi and D. W. Bahnemann, *Chem. Rev.*, 1995, **95**, 69–96.

4 K. Hashimoto, H. Irie and A. Fujishima, *Jpn. J. Appl. Phys.*, 2005, **44**, 8269.

5 Q. Guo, C. Zhou, Z. Ma and X. Yang, *Adv. Mater.*, 2019, **31**, 1901997.

6 K. Nakata and A. Fujishima, *J. Photochem. Photobiol., C*, 2012, **13**, 169–189.

7 U. I. Gaya and A. H. Abdullah, *J. Photochem. Photobiol., C*, 2008, **9**, 1–12.

8 I. Dhada, P. K. Nagar and M. Sharma, *Ind. Eng. Chem. Res.*, 2015, **54**, 5381–5387.

9 G. Li, D. Zhang and J. C. Yu, *Chem. Mater.*, 2008, **20**, 3983–3992.

10 Y. Sun, Z. Zhao, F. Dong and W. Zhang, *Phys. Chem. Chem. Phys.*, 2015, **17**, 10383–10390.

11 M. Spichiger-Ulmann and J. Augustynski, *J. Appl. Phys.*, 1983, **54**, 6061–6064.

12 W. L. Kwong, N. Savvides and C. C. Sorrell, *Electrochim. Acta*, 2012, **75**, 371–380.

13 W. Morales, M. Cason, O. Aina, N. R. de Tacconi and K. Rajeshwar, *J. Am. Chem. Soc.*, 2008, **130**, 6318–6319.

14 G. Hodes, D. Cahen and J. Manassen, *Nature*, 1976, **260**, 312–313.

15 Y. Guo, X. Quan, N. Lu, H. Zhao and S. Chen, *Environ. Sci. Technol.*, 2007, **41**, 4422–4427.

16 D. Le Bellac, A. Azens and C. G. Granqvist, *Appl. Phys. Lett.*, 1995, **66**, 1715–1716.

17 O. A. Balitskii, D. Moszynski and Z. Abbas, *RSC Adv.*, 2016, **6**, 59050–59054.

18 K. Manthiram and A. P. Alivisatos, *J. Am. Chem. Soc.*, 2012, **134**, 3995–3998.

19 S. Zhang, L. Zhang, S. Fang, J. Zhou, J. Fan and K. Lv, *Environ. Res.*, 2021, **199**, 111259.

20 C. Lu, J. Li, G. Chen, B. Li and Z. Lou, *Nanoscale*, 2019, **11**, 12774–12780.

21 R. T. Yadlapalli, R. R. Alla, R. Kandipati and A. Kotapati, *J. Energy Storage*, 2022, **49**, 104194.

22 B. K. Kim, S. Sy and A. Yu, in *Handbook of Clean Energy Systems*, John Wiley & Sons Ltd, USA, 2015.

23 Y. Zhou, H. Qi, J. Yang, Z. Bo, F. Huang, M. S. Islam, X. Lu, L. Dai, R. Amal, C. H. Wang and Z. Han, *Energy Environ. Sci.*, 2021, **14**, 1854–1896.

24 G. Wang, L. Zhang and J. A. Zhang, *Chem. Soc. Rev.*, 2012, **41**, 797–828.

25 E. Boateng, S. S. Thind, S. Chen and A. Chen, *Electrochem. Sci. Adv.*, 2021, **2**, e2100146.

26 W. Li, P. Da, Y. Zhang, Y. Wang, X. Lin, X. Gong and G. Zheng, *ACS Nano*, 2014, **8**, 11770–11777.

27 Y. Lu, J. Zhang, F. Wang, X. Chen, Z. Feng and C. Li, *ACS Appl. Energy Mater.*, 2018, **1**, 2067–2077.

28 B. Qu, A. Younis and D. Chu, *Electron. Mater. Lett.*, 2016, **12**, 715–731.

29 A. V. Salkar, S. V. Bhosale and P. P. Morajkar, in *Advances in Metal Oxides and Their Composites for Emerging Applications: A Volume in Metal Oxides*, ed. S. D. Delekar, Elsevier, The Netherlands, 2022.

30 P. Kubelka, *J. Opt. Soc. Am.*, 1948, **38**, 448–457.

31 C. C. Liao, F. R. Chen and J. J. Kai, *Sol. Energy Mater. Sol. Cells*, 2006, **90**, 1147–1155.

32 J. Tauc, R. Grigorovici and A. Vancu, *Phys. Status Solidi*, 1966, **15**, 627–637.

33 J. Tauc, in *Amorphous and Liquid Semiconductors*, Springer, Boston, MA, 1974, pp. 159–220.

34 B. A. De Angelis and M. Schiavello, *J. Solid State Chem.*, 1977, **21**, 67–72.

35 O. Hurtado-Aular, R. Anez, A. Sierraalta and J. Calderon, *Appl. Surf. Sci.*, 2020, **506**, 144719.

36 C. Lambert-Mauriat and V. Oison, *J. Phys.: Condens. Matter*, 2006, **18**, 7361.

37 O. Y. Khyzhun and Y. M. Solonin, *J. Phys.: Conf. Ser.*, 2007, **61**, 534.

38 W. Jiang, H. Loh, B. Q. L. Low, H. Zhu, J. Low, J. Z. X. Heng, K. Y. Tang, Z. Li, X. J. Loh, E. Ye and Y. Xiong, *Appl. Catal., B*, 2023, **321**, 122079.

39 T. L. Thompson and J. T. Yates, *Top. Catal.*, 2005, **35**, 197–210.

40 M. K. Nowotny, L. R. Sheppard, T. Bak and J. Nowotny, *J. Phys. Chem. C*, 2008, **112**, 5275–5300.

41 M. A. Oturan and J. J. Aaron, *Crit. Rev. Environ. Sci. Technol.*, 2014, **44**, 2577–2641.

42 J. M. Poyatos, M. M. Munio, M. C. Almecija, J. C. Torres, E. Hontaria and F. Osorio, *Water, Air, Soil Pollut.*, 2010, **205**, 187–204.

43 M. A. Rauf and S. S. Ashraf, *Chem. Eng. J.*, 2009, **151**, 10–18.

44 K. W. Park and A. M. Kolpak, *Commun. Chem.*, 2019, **2**, 79.

45 E. Alp, H. Eşgin, M. K. Kazmanlı and A. Genç, *Ceram. Int.*, 2019, **45**, 9174–9178.

46 A. F. Qasrawi, S. N. Abu Alrub and R. B. Daragme, *Opt. Quantum Electron.*, 2022, **54**, 449.

47 S. S. Kalanur, Y. J. Hwang, S. Y. Chae and O. S. Joo, *J. Mater. Chem. A*, 2013, **1**, 3479–3488.

48 Z. Liu, X. Yu, K. Wang, H. Yu, T. Wang, N. Zhao and J. Zhang, *J. Phys.:Conf. Ser.*, 2023, **2620**, 012055.

49 X. Zhang, M. Wang, X. Jia, K. Cao and M. Zhang, *ChemistrySelect*, 2019, **4**, 12785–12793.

50 E. Z. Kedves, E. Bardos, A. Ravasz, Z. R. Toth, S. Mihalydeakpal, Z. Kovacs, Z. Pap and L. Baia, *Materials*, 2023, **16**, 3621.

51 J. Liu, O. Margeat, W. Dachraoui, X. Liu, M. Fahlman and J. Ackermann, *Adv. Funct. Mater.*, 2014, **24**, 6029–6037.

52 J. A. Seabold and K. S. Choi, *Chem. Mater.*, 2011, **23**, 1105–1112.

53 J. Augustynski, R. Solarska, H. Hagemann and C. Santato, *Proc. SPIE*, 2006, **6340**, U140–U148.

54 Y. Oosawa and M. Grätzel, *J. Chem. Soc., Chem. Commun.*, 1984, **24**, 1629–1630.

55 R. S. Lillard, G. S. Kanner and D. P. Butt, *J. Electrochem. Soc.*, 1998, **145**(8), 2718–2725.

56 J. Zhao, E. Olide and F. E. Osterloh, *J. Electrochem. Soc.*, 2015, **162**(1), H65–H71.

57 G. Wang, Y. Ling, H. Wang, X. Yang, C. Wang, J. Z. Zhang and Y. Li, *Energy Environ. Sci.*, 2012, **5**(3), 6180–6187.

58 A. R. Bredar, A. L. Chown, A. R. Burton and B. H. Farnum, *ACS Appl. Energy Mater.*, 2020, **3**, 66–98.

59 J. R. Macdonald and W. B. Johnson, in *Impedance Spectroscopy: Theory, Experiment, and Applications*, ed. E. Barsoukov and J. R. Macdonald, Wiley & Sons Ltd, USA, 2018.

60 Z. Li, X. Yang, Y. Yang, X. Li, Y. Gao, L. Wang and W. Lü, *Chem. Eng. J.*, 2024, **498**, 155383.

61 M. Ö. A. Çolak, A. Güngör, M. Buldu-Akturk, E. Erdem and R. Genç, *Nanoscale*, 2024, **16**, 719–733.

62 A. Güngör, F. Bakan-Misirlioglu, R. G. Alturk and E. Erdem, *J. Energy Storage*, 2024, **76**, 110143.

63 Shreya, P. Phogat, R. Jha and S. Singh, *ACS Appl. Nano Mater.*, 2024, **7**, 8593–8611.